Additive Manufacturing 89 (2024) 104314

Contents lists available at ScienceDirect

Additive Manufacturing

journal homepage: www.elsevier.com/locate/addma

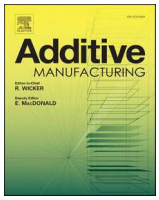

Continuous 3D printing of metal structures using ultrafast mask video projection initiated vat photopolymerization

Dylan Joralmon, Tengteng Tang, Sriram Rama Prakash, Harsh Verma, Stephanie Kim, Xiangjia Li *

Department of Mechanical and Aerospace Engineering, Arizona State University, Tempe, AZ 85283, United States

ARTICLE INFO

Keywords:
Additive manufacturing
Mask video projection
Vat photopolymerization
Metal precursors
Metal 3D printing

ABSTRACT

Additive manufacturing (AM) has recently emerged as the go-to technology for producing high-quality metal components to address cutting-edge research and industrial challenges. However, existing metal AM technologies operate on a layer-by-layer basis, giving rise to undesirable "staircasing effects" that result in the anisotropic behavior. Additionally, conventional metal printing methods are constrained by printing times, expensive hardware, and limited resolution control. In response to these limitations, this work is dedicated to the development of a cost-effective, ultra-fast layerless metal AM process for crafting intricate 3D metal structures. Low viscous resin was developed to enable continuous printing of metal precursors via mask video projection-based vat photopolymerization, which enable tunable physical properties and superior surface quality. Based on experimental findings, high-density meso- and microscale metallic parts can be printed at speeds orders of magnitude faster than commercial metal AM technologies. Furthermore, printed metallic components display a uniform morphology and microstructure with consistent grain size distribution. A comparative analysis of the surface quality between layer-based and layer-less printed metal structures were conducted. This work has the potential to revolutionize not only the field of AM but also various industries reliant on high-quality metal components, such as aerospace, automotive, and medical devices.

1. Introduction

Metal additive manufacturing (AM), also known as metal three-dimensional (3D) printing, has recently demonstrated the ability to fabricate geometrically intricate and unique metal and metal alloy objects, with feature sizes ranging from macro to nanoscale structures, when compared to traditional manufacturing technologies [1–4]. The design flexibility and material selection provided by AM technologies enables the fabrication of metal components with complex geometry and excellent physical properties for use in automotive, aerospace, and biomedical industries [5–7]. For example, selective laser melting (SLM) and powder bed fusion (PBF) technologies have exhibited the capability to fabricate high strength, impact resistant metal 3D objects, with lattice structures, which can withstand extreme thermal environments under high mechanical loading [8,9]. Furthermore, recent advancements in extrusion- and energy deposition-based metal rapid prototyping technologies have shown that functionally graded materials, such as electrodes and heat exchangers, with excellent electrical and thermal conductivity can be manufactured with relative ease allowing for rapid and efficient topologically optimized designs via machine learning [10,11]. Currently, metal AM technologies can be classified into two discrete regimes based primarily on how the digital model is converted into a physical structure by the deposition of material along a predetermined tool path. Material deposition techniques, such as electron beam melting (EBM) and direct ink writing (DIW), trace a computer-generated tool path to form the metal structures layer-by-layer while simultaneous material deposition processes, such as metal binder jetting (MBJ), employ a selectively controlled surface energy and material deposition tools to construct a single layer instantaneously [12]. However, since the 3D metal structure is constructed layer-by-layer, a conspicuous “staircasing effect”, related to the layer thickness resolution used to generate the tool path or 2D mask images, will significantly influence the surface roughness of the manufactured part, leading to detrimental effects on the desired functionality [13]. High surface quality metal structures are imperative for applications in electronic devices, optical components, and aerodynamic structures, which impose strict

* Corresponding author.
E-mail address: xiangjia.li@asu.edu (X. Li).

https://doi.org/10.1016/j.addma.2024.104314
Received 21 February 2024; Received in revised form 11 June 2024; Accepted 18 July 2024
Available online 19 July 2024

tolerances on surface roughness, where required for adequate performance of the metal part [14]. Moreover, challenges associated with obtaining excellent layer adhesion, using traditional layer-based metal printing technologies, promotes anisotropic behavior of the metal structure, from non-homogeneous physical properties observed in individual layers, which has been found to compromise thermal, electrical, and mechanical properties [12,15]

Recent developments in AM technologies that utilize vat photopolymerization (VPP), a method that integrates a 2D light beam to solidify selective areas of a photocurable liquid resin layer-by-layer, has made significant improvements in both fabrication speed and surface quality of 3D printed metal, ceramic, and polymer composite structures [12,15,16]. Digital light processing (DLP) and stereolithography (SLA), two types of vat photopolymerization (VPP) techniques, have currently demonstrated the ability to manufacture high temperature refractory metals and multi-material structures for high performance electrodes with good surface quality and greater resolution when compared with laser energy deposition approaches [17,18]. However, ceramics and metals precursors printed via current VPP exhibit limited printing speed due to the material recoating and exhibit anisotropic grain morphology which could cause the formation of defects and microcracks during post-processing [18]. Conversely, continuous liquid interface production (CLIP) is a continuous AM approach that implements an oxygen rich dead zone and 2D light projection to fabricate homogeneous 3D object with smooth surface features. Since photocurable material continuously refills the fabrication area above the thin oxygen inhibition region, the CLIP process can achieve printing speeds substantially greater than layer-based AM technologies with excellent dimensional accuracy and small feature size [19–22]. In CLIP, low viscous printing resin promote adequate recoating of photocurable material, to attain fast build times [20,21]. However, in order to achieve dense metallic objects, a high solid loading content of metal precursor powders to a polymer matrix which consequently increases the viscosity of the material, while simultaneously decreasing the light penetration depth and photosensitivity of the material, making it incompatible with layer-less AM processes [18]. Therefore, challenges of incorporating metal powders to obtain a low viscous printing ink for the continuous printing of metal precursors remains to be addressed.

Inorganic metal salts, as a metal precursor additive, have shown promising rheological properties and steric stability when combined with low viscosity acrylic-based resins for metal printing [23]. Metal salts are predominantly low-cost and can be incorporated into photocurable slurries, with excellent refractive indices, high solid content, and particle dispersion, allowing for the rapid fabrication of robust, high-resolution metal structures, via subsequent oxidation and reduction post-processing methods, for a broad range of metals and alloys [23]. Furthermore, inorganic metal salts show great advantages for the fabrication of homogeneous metal-doped polymer derived ceramics via VPP with high dimensional accuracy [24]. Besides, the methodology for manufacturing metal oxide and metallic structures via metal salt precursors is extraordinarily sustainable. Base metal salt precursor material can be easily synthesized from metal oxide and metallic structures, using rudimentary acid metal chemical reactions, and repurposed for the fabrication of a new metallic part which provides new perspectives on the iterative design of metal 3D printed structures. In contrast to conventional metal precursors, microscale hydrogel scaffolds have demonstrated the capability to fabricate metal and multi-metal components, in parallel, through ionic diffusion into the polymeric matrix [25]. This significantly eases challenges associated with optimizing resin formulations and printing parameters for individual slurries since only the solvent needs to be changed for different metals and alloys [25]. However, since the hydrogel structure must be immersed in a metal solvent to promote the exchange of metal ions, constructing geometrically complex and intricately patterned multi-metal structures remains an issue. Furthermore, the aforementioned metal DLP techniques are layer-based approaches which evinces reduced surface quality at microscales and nonhomogeneous physical properties from weak interface adhesion between adjacent layers [26]

In this work, we present a novel low-cost and layerless metal AM process to rapidly fabricate high resolution 3D metallic structures with homogeneous, isotropic physical properties and smooth surface finish. As depicted in Fig. 1a, the mask video projection-based vat photopolymerization (MVP-VPP) process circumvents material and printing speed limitations of current metal AM technologies by integrating a low viscosity metal salt precursor resin (see Fig. 1b) and high frame rate video, generated from the digital model, that uniformly deposits and crosslinks new material in the projection area promoting the continuous fabrication of 3D metallic precursors. Firstly, curing characterization and rheological behavior was investigated to ascertain optimal fabrication speeds based on resin refilling speed and photopolymerization mechanisms. Optimized post-processing parameters, guided through thermogravimetric analysis (TGA), were evaluated with the purpose of efficiently converting the printed structure into the desired metallic structure via debinding, sintering, and thermal reduction, see Fig. 1c. Based on experimental results, this process has demonstrated the ability to fabricate dense, homogenous metal objects within minutes at micron resolution, exhibiting drastically improved surface roughness compared with current layer-based metal AM processes. Moreover, unprocessed materials are cost effective, easily procurable, and readily recyclable which make this an ideal metal AM method for the design of sustainable, next-generation functional metal devices with isotropic physical properties.

2. Material and methods

2.1. Material preparation

2.1.1. Pre-processing of anhydrous metal sulfate

In order to achieve a high concentration of metal sulfate particles within the polymer matrix, copper sulfate pentahydrate (≥98.0 %, Sigma Aldrich) was first dehydrated to form anhydrous copper sulfate ($CuSO_4$). Dehydration was performed using a muffle furnace (MTI KSL-1700X, MTI Corp.) and alumina crucibles with a ramping rate of 5 ° C min^{-1}, target temperature of 400 ° C, and a dwell time of 5 hours. After furnace cooling, the mass of the resulting powder was ascertained by a high precision balance to verify water molecules were adequately removed from the raw material based on thermogravimetric data. Anhydrous metal sulfate powder with particle size distribution less than 100 μm was achieved by sieving metal sulfate through a 0.1 mm metal mesh (TITAN) before being used as the filler material. The particle size of $CuSO_4$ after milling was approximately 1 μm (see Figure S1 in the supporting information).

2.1.2. Preparation of metal sulfate resin

Organic monomers 1,6-Hexanediol diacrylate (HDDA) (80 %, Sigma-Aldrich) and trimethylolpropane ethoxylate triacrylate M_N = 428 (E-TMPTA) (Sigma-Aldrich) were mixed utilizing a mass-to-mass ratio of 22–3, respectively, with different weight percentages of photoinitator (Omnirad 819, IGM) for a minimum of 3 hours using a magnetic stirrer. To improve the curing performance and rheological properties of the metal salt resin, the dispersant Triton X-100 (TX-100) (Sigma-Aldrich) was added to the solution and allowed to homogenize for 1 hour. The anhydrous metal salt powder was then batchwise added to the photocurable resin and dispersant solution in a stainless-steel milling jar with zirconia milling balls at a speed of 300 RPM overnight using a planetary ball mill machine (MTI MSK-SFM-1). The mass of anhydrous metal salt was adjusted to produce photocurable metal salt bearing resins with weight percentages ranging from 40 % to 67 %.

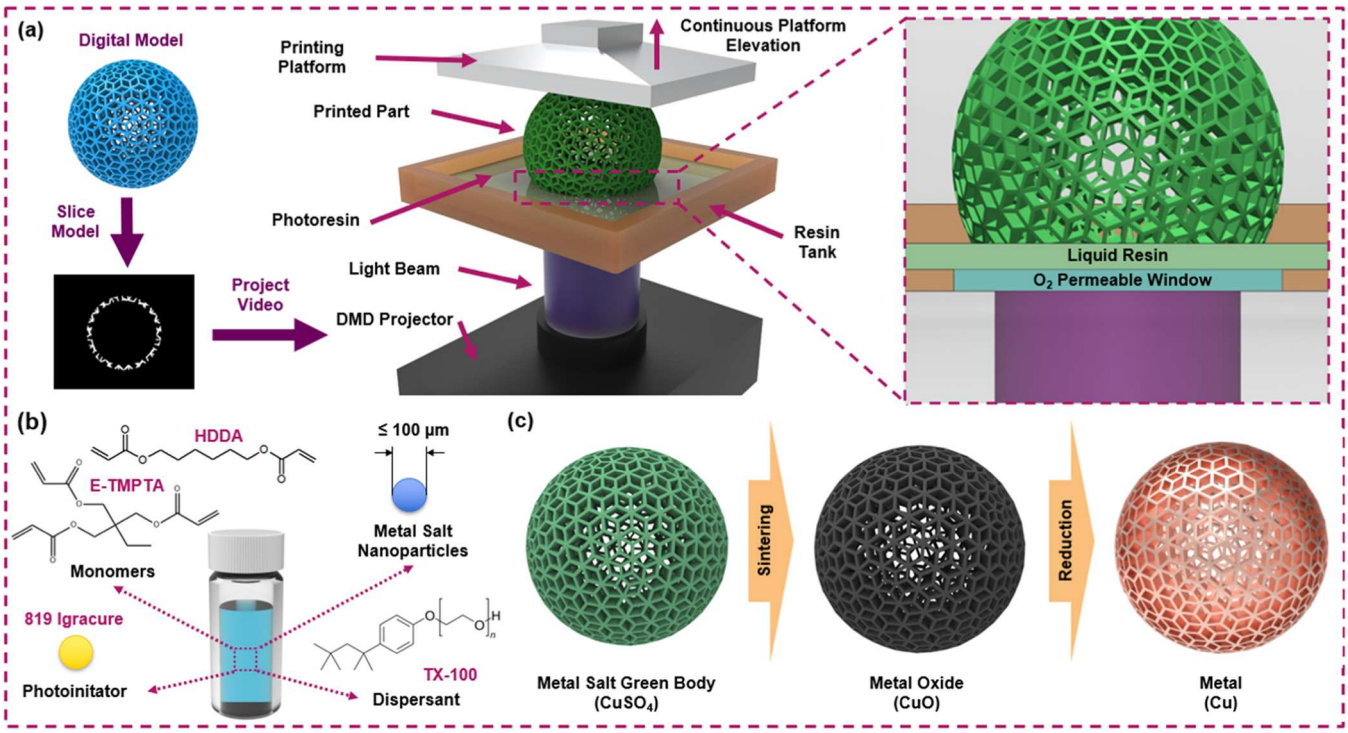

Fig. 1. Overview of the MVP-VPP methodology showing the (a) fabrication workflow of the MVP-VPP process from digital model to 3D printed object; (b) depiction of metal precursor printing resin with monomer, dispersant, photoinitiator, and metal salt constituents; and (c) the thermal synthesis process for transforming 3D printed green body into metal structures using copper as the primary example.

2.2. Mask video projection initiated vat photopolymerization

2.2.1. Video construction

Utilizing homemade STL slicing software, digital models are imported and centered on the printing platform before being converted into a collection of grayscale mask images that each represent a cross-sectional area of the overall structure. Grayscale images are then processed through a video editor (VirtualDub64) to construct a mask image video of the digital model where the frame rate, represented here in frames per second (fps), is tuned to synchronize with the linear motion of the build platform during the printing process determined by Eq. (6). In this work, a conservative slicing thickness of 5 µm was utilized for the fabrication of all digital models in order to improve surface roughness.

$$fps = \frac{printing\ speed}{slicing\ thickness}\# \tag{6}$$

2.2.2. Fabrication of metal precursors

In the MVP-VPP process, photosensitive metal salt resin continuously recoated the projection area in a transparent, PDMS-coated glass resin tank as the printing platform elevated at a constant velocity. As the printing platform continuously moves upwards, each cross-sectional area of the target object is selectively cured forming a solid body, above the boundary of the oxygen inhibition region, when a 2D patterned light source is projected by the optical system onto the bottom of the glass tank. To project the mask image video as a 2D light beam, a 405 nm wavelength light was reflected by a digital micromirror device (DMD), composed of an array of 1920 ×1080 micromirrors, and focused by a convex lens (Thorlabs Inc.) with a focus distance f = 150 mm.[36,37] Cross-linking characteristics of metal salt resins were performed by solidifying thin films (2 mm×2 mm) which were subsequently measured using high-precision calipers (EAGems Digital Caliper) to determined cure depths and exposure times for the purpose of setting printing parameters. To study the influence of printing speed on maximum allowable side length, a digital model composed of an array of squares, with lengths ranging from 0.8 to 2 mm, was generated using SolidWorks and converted into a mask projection video (Section 3.2.1). The printing speed of the MVP-VPP process was adjusted based on the photosensitivity and rheological properties of the metal salt material to improve dimensional accuracy and surface finish of printed metal precursors. Metal precursors printed through the MVP-VPP process were washed in HDDA for 15 minutes using an ultrasonicator and dried under vacuum for 1 hour. Printed metal precursors were then fully cured by prolonged exposure to a UV lamp to promote crosslinking of residual uncured resin on the surface of the metal precursors.

2.3. Characterization of metal sulfate resin and 3D printed structures

2.3.1. Rheological measurements

Viscosity experiments of the metal salt resins were performed at room temperature using a rheometer (Discovery HR 30) to analyze the rheological behavior of the material. Steady-state shear rate sweep, from 10 to 100 s^{-1}, was conducted on the resin, with varying concentration of anhydrous metal salt and dispersant, directly after wet milling. With the purpose of preventing solidification of metal sulfate resin during testing, PI was intentionally omitted during material preparation.

2.3.2. Thermogravimetric analysis

Thermogravimetric analysis (TGA) was conducted on cubic green body samples using a simultaneous temperature analyzer (LABSYS evo) utilizing a target temperature of 1000 ° C with a ramping rate of 5 ° C min^{-1} under an air atmosphere. The derivative of mass loss (DTG) was then calculated from TGA data and used to generate debinding and sintering curves for thermal post-processing based on inflection points.

2.4. COMSOL simulation of liquid resin flow

The laminar flow module of COMSOL Multiphysics is used to analyze the refilling process of liquid and particle mixture during MVP-VPP printing. The liquid filling process is simplified as sheet liquid filling.

In the setting of boundary conditions, the bottom surface of the printed sample that moves upwards is replaced by the fixed upper surface, and is set as a liquid outlet, while the four narrow sides of the thin plate are selected as inlets. Obviously, different lifting speeds correspond to different inlet fluid velocities. By observing the process of printing a constant-section (10 mm×10 mm) structure, the process of fluid refilling is simplified to a thin plate with a filling gap of 0.1 mm, the top of the thin plate is an outlet, the pressure is 0 Pa, and the flow velocity of the inlets on the four sides is determined by the lifting speed. Streamlines in simulation results reveal liquid and particle refilling states and locations of potential cavity defects.

2.5. Post-processing of 3D printed metal salt precursors

Final metal parts were obtained from TGA-assisted thermal processing that consists of three steps: debinding, sintering, and thermal reduction of the printed metal precursors using the MVP-VPP process. Debinding was performed in a tube furnace, under inert atmosphere, utilizing a conservative ramping rate of 1 ° C min^{-1} with dwell temperatures of 215 ° C, 360 ° C, 415 ° C, and 600 ° C for 2 hours. The samples were then placed in a muffle furnace and thermally decomposed to metal oxide in alumina crucibles in air at dwell temperatures of 705 ° C and 785 ° C for 2 hours. Afterwards, the temperature was increased further to reduce porosity via sintering of the samples under different temperature conditions of 850 ° C, 925 ° C, and 1000 ° C for 5 hours. The resulting metal oxide structures are then thermally reduced in a tube furnace to metal under 5 % H_2/Ar atmosphere at a temperature of 800 ° C for 10 hours using a ramping rate of 3 C° min^{-1}.

2.6. Thermal characterization

Heat dissipation of metal parts fabricated using the MVP-VPP process was demonstrated by heating the base of the printed heat sink to 110 ° C on a hot plate. Infrared videography (FLIR ONE Gen 3) was then utilized to observe the temperature distribution and heat dissipation throughout the lattice structure during the experiment. COMSOL Multiphysics was utilized to analyze the thermal distribution in the digital lattice models for comparison with laboratory experiments using a boundary condition of 110 ° C on bottom plate.

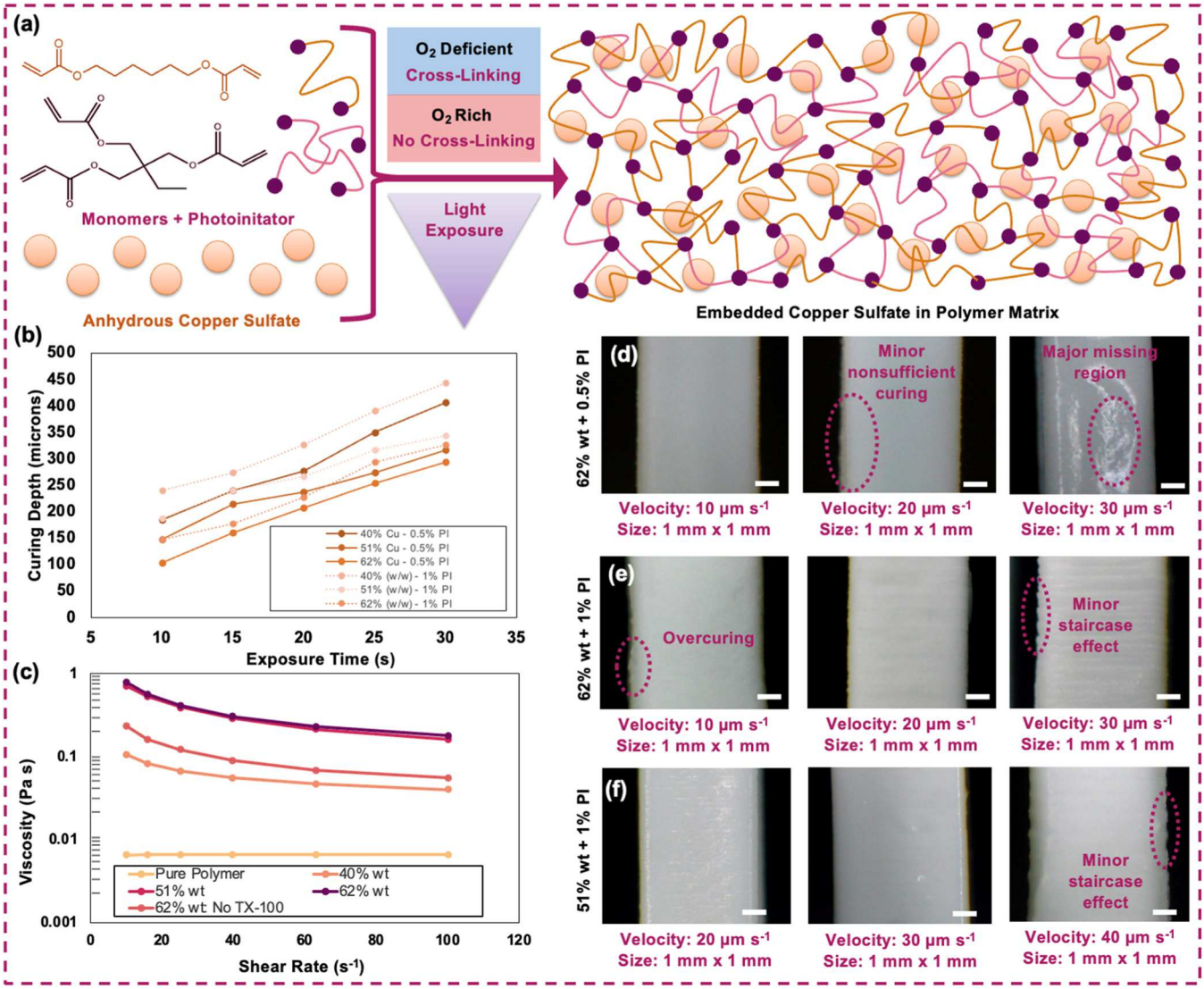

Fig. 2. Material characterization and printing performance of metal salt resins illustrating (a) the cross-linking mechanism for encapsulating metal salt particles; (b) curing characterization and (c) apparent viscosity of metal salt resin with different solid loading; (d), (e), and (f) surface quality of specimens with varying concentrations of metal salt loading printed via MVP-VPP at different printing speeds. Scale bars are 200 µm.

3. Results and discussion

3.1. Continuous printing of metal precursors via MVP-VPP

3.1.1. Material curing characterization

Inorganic metal salts can readily be dispersed in acrylate-based polymers, along with a photo-initiator (PI), for the continuous printing of 3D metal precursors through the MVP-VPP approach. Selective cross-linking of organic monomers occurs through free radical photo-polymerization, upon incident light exposure of the 2D pattern light beam, in regions on the metal salt resin that are oxygen deficient to obtain a homogeneous distribution of encapsulated metal salt particles, see Fig. 2a. From this depiction, as the loading of metal salt particles increases, the number of mean pathways for light to penetrate the material and promote the photopolymerization process decreases since the light is scattered by metal salt particles. Curing characteristics of the printing resin with different PI concentrations and solid loadinsg of metal salt (CuSO4 particles) was investigated for the fabrication of metal precursors using the MVP-VPP. The required exposure time and resulting curing depth were heavily influenced by the dispersion of metal salt and photosensitivity of the polymeric matrix. As depicted in Fig. 2b, with a 20-second exposure time, the curing depth of photoresin containing 51 % (w/w) $CuSO_4$ particles increased from 236 μm to 267 μm as the PI concentration increased from 0.5 % (w/w) to 1 % (w/w). Additionally, increasing the $CuSO_4$ loading from 40 % (w/w) to 62 % (w/w) resulted in a significant reduction in curing depth by approximately 100 μm for both the 0.5 % (w/w) and 1 % (w/w) PI materials at each exposure time. An accurate mathematical model was utilized to express the relationship between energy distribution and light penetration for determining the curing depth of metal salt-based resin. The proposed curing model for the MVP-VPP process can be evaluated through the working principle of Jacobs, using Eq. (1) where *Dp* is the penetration depth in the metal salt-based printing resin where the light intensity decreases gradually to e^{-1} of the light intensity at the bottom of the resin vat, *E0* is the energy at the surface of the material, and E_{Cr} is the critical energy requirement necessary to initiate the photo-polymerization process. [27,28]

$$C_d = D_p \ln\left(\frac{E_0}{E_{cr}}\right) \tag{1}$$

Additionally, experimental results show that increasing the solid loading of $CuSO_4$ particles extends the exposure time required to adequately cure a thin film of material with the same thickness. For example, at a constant light intensity, an exposure time of 10 seconds is needed to cure 40 % (w/w) $CuSO_4$ resin, whereas 14 seconds is required for 62 % (w/w) $CuSO_4$ resin. A similar trend is observed in printing materials with higher PI concentrations; however, shorter exposure times are needed compared to the resin with 0.5 % (w/w) PI. As more CuSO4 particles are added into the polymeric matrix, the mean distance between adjacent particles decreases significantly resulting in light scattering effects that prevent the 2D patterned light beam from penetrating the photocurable resin to promote the photopolymerization process. Therefore, the apparent viscosity of the material used to quantify the impact of dispersant on rheological stability is closely related to the photosensitivity of the printing material, where higher viscosities resulting in longer exposure times and smaller curing depths when compared to pure photocurable resin. Consequently, the exposure times and curing depths were used to set the printing speed for the continuous printing of high-resolution metal precursors with smooth surface finish via the MVP-VPP.

3.1.2. Rheological behavior

The rheological behavior of metal salt resins under different solid loading conditions of metal salt (CuSO4 particles) was studied using a shear rate sweep test from 10 s^{-1} to 100 s^{-1}. Apparent viscosity of the resin was significantly impacted by the loading of CuSO4 particles and the addition of the dispersant Triton X-100 (TX-100) into the polymeric matrix. The primary role of the dispersant is to generate a stable printing ink by preventing agglomeration of adjacent metal sulfate particles within the polymer solution via hydrophobic and hydrophilic interactions between the solid and liquid phases. As shown in Fig. 2c, when the loading of CuSO4 particles is increased from 40 % (w/w) to 62 % (w/w), the viscosity increases from 0.068 Pa/s to 0.41 Pa/s for a shear rate of 25 rad/s. Furthermore, the apparent viscosity of resins with 51 % (w/w) and 62 % (w/w) CuSO4 loading were nearly identical, indicating that increasing CuSO4 particles up to the maximum threshold has a negligible effect on the materials viscosity. The observed shear rate sweep curves for all CuSO4 bearing resins exhibit shear thinning behavior, when compared with pure resin, since higher shear rates promote deagglomeration of CuSO4 clusters which subsequently lowers the viscosity of the material. Furthermore, low viscous printing resins, within the range of 10^{-1} to 10^{-2} Pa/s, can be achieved, so that the liquid phase can more readily recoat the bottom surface of the resin and deliver microparticles homogeneously to the fabrication area, improving the mean resin refilling speed.

Comparison of printing resin containing 62 % (w/w) CuSO4 particles resin with and without the dispersant TX-100 demonstrates the effect of dispersant on rheological stability of the resin during the continuous printing process. Shear sweep curves decrease slightly from 0.80 to 0.24 Pa/s for resin with and without TX-100 at a shear rate of 10 rad/s, respectively. However, CuSO4 based printing resin without TX-100 is highly unstable and spontaneously flocculates within minutes, forming large aggregates of CuSO4. Agglomerations present within the CuSO4 based resin without TX-100 during continuous printing can alter the materials local viscosity and photosensitivity resulting in poor structural integrity, body defects, and low-resolution printed quality. Although separation can also be observed in CuSO4 printing resins containing TX-100, the onset of sedimentation is typically on the timescale of hours. Furthermore, dispersant carrying resins can be readily homogenized and utilized in the MVP-VPP process, showing improved printability and shelf-life of dispersant carrying CuSO4 resins. Consequently, the 62 % (w/w) CuSO4 with TX-100 exhibited low apparent viscosity, high solid loading percentage, and good rheological stability, this material can be incorporated into the layer-less printing of 3D metal precursors via MVP-VPP.

3.1.3. Surface quality

To optimize the printing parameters of the MVP-VPP process, the influence of printing speed and photosensitivity on the surface quality of printed metal sulfate structures was investigated. A 2D light beam in the pattern of a 1 mm×1 mm square was reflected by the optical system on the surface of the photosensitive metal sulfate resin while the velocity of the linear stage was set between 10 μm/s and 30 μm/s. As depicted in Fig. 2d, 62 % (w/w) CuSO4 based resin with 0.5 % PI showed excellent surface roughness and high cross-linking ratio for printing speeds up to 20 μm/s; however, beyond this threshold the fabricated samples began to exhibit substantial dimensional deviations from the target 3D design. For example, setting the printing speed to 30 μm/s resulted in body structures with missing portions on the surface due to insufficient monomer cross-linking within the material. Additionally, experimental results showed that increasing the PI concentration to 1 % (w/w), while maintaining the same solid loading of $CuSO_4$, worsened the surface quality for samples fabricated at a velocity of 10 μm/s, exhibiting characteristics of overcuring (see Fig. 2e). For the same material, the dimensional accuracy and surface quality improved when specimens were printed at linear velocities of 20 μm/s via MVP-VPP. Increasing the printing speed to 30 μm/s partially mitigated the missing cured portions seen in the 0.5 % (w/w) PI solution, although a conspicuous "staircasing effect" indicated that the material was not fully cross-linked. As depicted in Fig. 2f, reducing the solid loading of $CuSO_4$ from 62 % (w/w) to 51 % (w/w) significantly improved the surface quality of the material with

1 % PI, even at a printing speed of 20 μm/s. The surface of samples printed using 51 % (w/w) and 1 % PI, the surface turns much smoother when the speed increased to 30 μm/s. However, printing speeds greater than 30 μm/s exhibited a higher risk of micropore and staircasing defects due to insufficient resin filling during the printing of larger cross-sectional areas. Therefore, MVP-VPP printing parameters must be constrained by both the rate of liquid refilling and photocuring within the boundary of the projection area. To validate the liquid refilling postulation, a mathematical model was constructed and compared against a series of experiments and simulations which are presented in the following section.

3.2. Printing speed investigation

3.2.1. Resin refilling

In the MVP-VPP, an oxygen inhibition layer, which prevents photopolymerization upon incident light exposure, is formed through the diffusion of oxygen molecules from a thin film of polydimethylsiloxane (PDMS) into the resin which promotes the fabrication of 3D structures continuously [20]. As illustrated in Fig. 3a, as the build platform moves with a constant vertical velocity Vz, the cured metal precursor, with square side length L, is elevated above the oxygen inhibition layer by a small gap distance h. Based on previous work, resin refilling within the video projection area is primarily driven by the positive pressure gradient between the ambient air pressure and void left from the cured part coupled with the effect of gravity on microparticles embedded within the resin [20]. During liquid refilling, it is assumed that the surface boundary of the oxygen inhibition layer and the cured structure are both parallel, with respect to each other, and remain unperturbed during both resin filling and solidification processes for the entire printing duration. Furthermore, the resin flow during printing is assumed to be laminar, steady, and fully developed. Consequently, the velocity profile can be characterized as Hele-Shaw flow by Eq. (2) where V_R is the velocity of the resin, Δp is the local pressure gradient, z is the spatial coordinate in the z-direction, and μ is the viscosity of the liquid resin.[29]

$$V_R = \frac{\Delta p}{\mu L}\left[\left(\frac{h}{2}\right)^2 - \left(z - \frac{h}{2}\right)^2\right] \tag{2}$$

Although the velocity determined through Eq. (2) is adequate in characterizing the localized resin refilling dynamics during the continuous printing, it neglects the monomer cross-linking reaction engendered from incident light exposure on the resin surface. Metal salt resin recoats the projection area where the viscosity increases substantially during cross-linking of monomer constituents [30,31]. Therefore, Eq. (2) can be modified to incorporate the exponential decay of viscosity due to the photopolymerization process during liquid refilling, as shown in Eq. (3), where α is a non-zero constant if light energy is absorbed by the metal sulfate resin.

$$V_R = \frac{\Delta p}{\mu L} e^{-\alpha}\left[\left(\frac{h}{2}\right)^2 - \left(z - \frac{h}{2}\right)^2\right] \tag{3}$$

Inspection of Eq. (3) reveals that resin refilling speed in MVP-VPP increases with smaller side lengths, lower viscosity, and larger oxygen inhibition thickness, allowing for faster printing times. Conversely, the refilling velocity will decrease dramatically for resins with high viscosity and low energy absorption from light scattering effects. Moreover, resins used in this work require excellent dispersion of metal salt particles to prevent premature hydration and aid in transporting a sufficient amount of the solid phase to the fabrication area by the liquid phase. Thus, in order to increase the mean resin refilling and printing speed, the height of the oxygen inhibition zone can be increased, while simultaneously integrating low viscosity printing materials with superior dispersion to

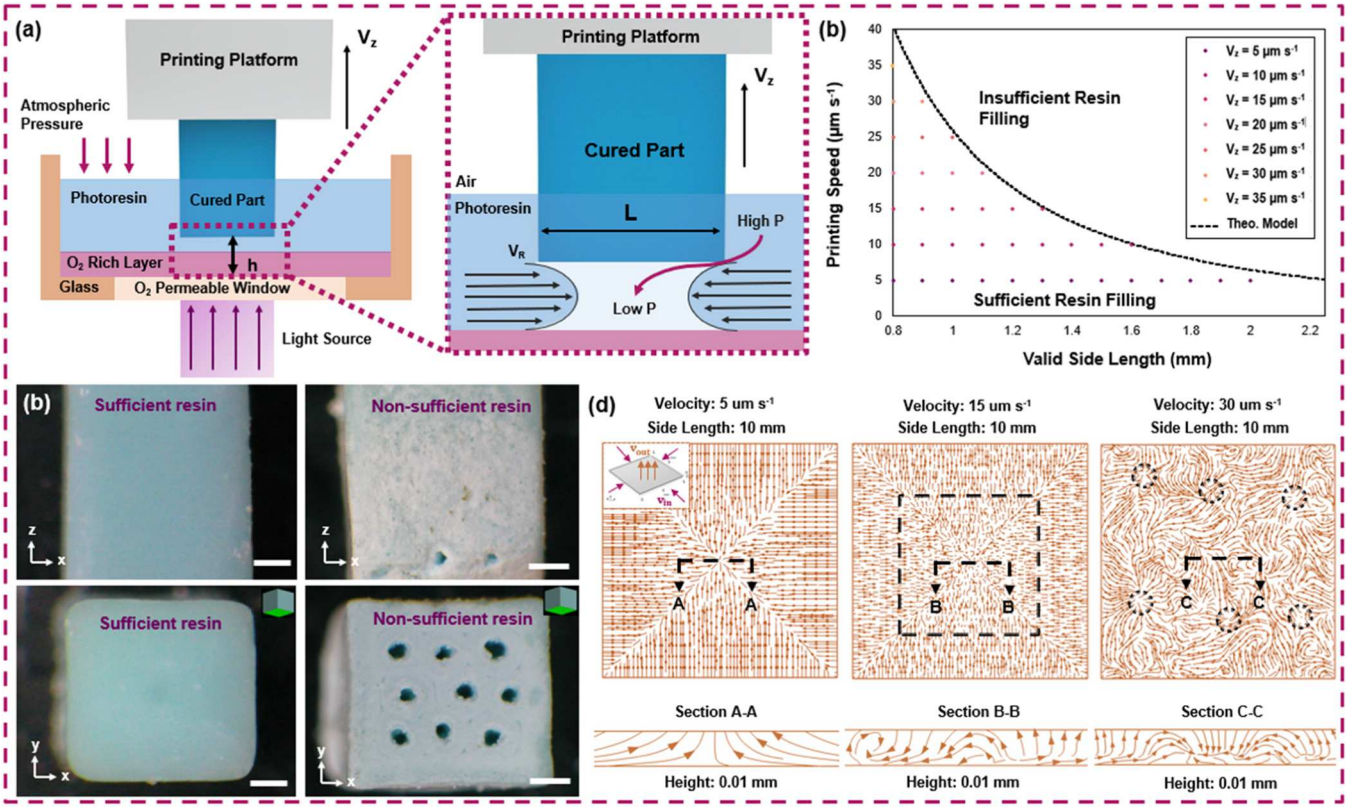

Fig. 3. Self-recoating in MVP-VPP illustrating (a) continuous resin flow during part fabrication; (b) front and top view of cubic structures with different side dimensions displaying surface quality for sufficient and insufficient resin refilling; (c) valid side length of fabricated parts during continuous resin refilling under different printing speed; (d) simulation of continuous resin flow utilizing different printing speeds. Scale bars: (b) 200 μm, 400 μm (left to right).

enable larger fabrication areas [19]

To generate an accurate model that characterizes the relationship between liquid refilling and maximum fabrication area, the volumetric flow rate of metal salt resin to the fabrication area during the MVP-VPP was studied. As the cured structure is continuously lifted, the volumetric flow rate Q under a square cross-section with area L^2 can be described:

$$Q = \int_0^L dx \int_0^h \frac{\Delta p}{\mu L} e^{-\alpha} \left[\left(\frac{h}{2}\right)^2 - \left(z - \frac{h}{2}\right)^2 \right] dz \tag{4}$$

Since the printing platform is moving with constant velocity Vz, the total volume under the cured part, after time increment Δt, must be sufficiently filled with resin, and subsequently photopolymerized, to achieve continuous fabrication of metal salt structures. Inadequate resin filling, for an arbitrary projection area A, should then be distinguishable by voids or channels in the final cured structure. Hence, the maximum side length L_{max} that can be printed for a given printing speed using MVP-VPP is detailed in Eq. (5), where K is a constant that encompasses contributions from the pressure gradient, oxygen inhibition layer height, and apparent viscosity of the resin.

$$L_{\max} = \frac{K}{\sqrt{V_z}} e^{-\alpha} \tag{5}$$

Accordingly, the theoretical model expressed in Eq. (5) is refined through experimental testing of the resin refilling process to probe the relationship between printing speed Vz and maximum side length L_{max}. Based on curing characteristics described in previous sections, an array of squares with side lengths ranging from 0.8 mm to 2 mm, in 0.1 mm increments, were printed using the MVP-VPP process with different speeds. Successfully printed structures exhibit excellent surface roughness with no defects in contrast to defective printed structures, which are distinguished by pore defects on the front and top faces of the cubic structure, see Fig. 3b. Printing speed was gradually increased from a baseline velocity of 5 μm s^{-1} to the printing speed at which no successful printed parts were printed. Experimental results are illustrated in Fig. 3c with the theoretical model superimposed where the constants K and α are empirically determined through nonlinear curve fitting analysis with the constants equal to 3.2 and −0.4637, respectively. The theoretical model presented here can be employed to predict defects in the printed structure based on the cross-sectional area of the digital model, where fabrication areas and velocities that lay underneath the theoretical model curve will result in sufficient resin filling during printing. Conversely, faster printing speeds with large fabrication areas will increase the probability of micropore defects since the resin refilling and cross-linking are not sufficient.

3.2.2. Simulation of continuous resin flow

In order to predict the influence of printing speed on the void defect at the bottom of the printed part, we used the computational fluid simulation module of COMSOL Multiphysics to uncover the mechanism of defect formation in MVP-VPP. The simulation results show that the liquid filling streamline under the condition of low lifting speed is laminar flow, and the liquid carries the microparticles to uniformly and stably fill the void gap generated by continuous lifting, see Fig. 3d. When the lifting speed increases, the streamlines at the center of the thin plate gradually become unstable and excessively turbulent. When the lifting speed exceeds a certain threshold, the filling streamline is completely disordered, and the corresponding discontinuous homogeneous supply of particles and sudden changes in flow rate leads to a significant increase in the probability of cavity defects, which is detrimental to controlling print quality and should be avoided.

3.3. Morphology and density evaluation

3.3.1. Thermal formation of metal microstructures

With the purpose of obtaining geometrically complex copper structures with excellent surface roughness, the influence of post-processing including debinding, sintering, and thermal reduction, on the structural integrity of MVP-VPP printed metal precursors are evaluated. In contrast to conventional DLP washing techniques that utilize volatile washing agents such as isopropyl alcohol (IPA), metal precursors printed through our process are hygroscopic and consequently are washed in a solution of HDDA to prevent swelling and surface defect formation before thermal processing. Metal precursors that are ultrasonicated in HDDA maintain their morphology after washing and exhibit good surface roughness when compared to printed parts ultrasonicated in IPA that results in the swelling of the overall structure and poor surface roughness from the presence of $CuSO_4$ aggregates (Figure S1, Supporting Information). Consequently, printed metal precursors are dried under vacuum before post-processing to prevent hydration from the ambient atmosphere that may compromise the overall accuracy of the final metal component. As shown in Fig. 4a, mesoscale gyroid structures with smooth features were obtained through stable thermal decomposition of printed metal precursors to form metal oxide structures which are then subsequently thermally reduced, under a reducing gas (5 % H2 / 95 % Ar), to transform the metal oxide structures into a dense, monolithic metal component.

Optimization of debinding and sintering temperature profiles was conducted based on TGA results to reduce the decomposition rate of monomers, dispersant, and PI within the printed metal precursors. Shown in Figure S2, there exist three distinct regions where significant mass loss occurs: 100–200 °C, 300–500 °C, and 700–800 °C. In the low temperature regions, dispersant and monomer constituents are decomposed and flushed out by the carrier gas, resulting in a mass loss of 56 %, which is then followed by the thermal decomposition of sulfide from $CuSO_4$ to copper oxide (CuO) in the high temperature region further reducing the overall mass loss to 72 %. Therefore, successful debinding, sintering, and thermal reduction of printed metal precursors using the MVP-VPP process must consider the thermal decomposition kinetics from dispersant and monomer removal, in addition to stable metal oxide synthesis, sintering, and reduction, in order to retain the surface quality of 3D printed metal objects.

During debinding and sintering, furnace temperature must be incrementally increased to prevent vigorous outgassing of dispersant and monomer constituents which can lead to the formation of macrocracks in the CuO part. A constant flow of inert gas, during debinding, carries volatile, organic material from the surface of the printed metal precursors to reduce rapid thermal processes and promotes stable decomposition of $CuSO_4$ green bodies. Once the organic material is completely expelled, sintering is performed, in an oxidizing environment, to remove any residual carbon on the surface such that oxygen can react with $CuSO_4$ particles and easily convert the structure to metal oxide without compromising the surface integrity. Once the CuO part is obtained, the part is then placed in a reducing atmosphere to form the final Cu structure. In order to verify the composition of the final metal part, elemental mapping of MVP-VPP printed octahedron pyramid evinces that the majority of the chemical composition is Cu with small contributions from C, Si, and O. Cu contributes 89.1 % weight to the overall structure in comparison to other elements such as C and O which are around 10.1 % and 0.6 % in weight, respectively (Figure S3, Supporting Information). The presence of increased amount of C in the final metal structure can be attributed to extrinsic carbon imparted from managing the Cu objects during sample loading onto the SEM instrument.

3.3.2. Influence of sintering temperature on microstructure and density

With the aim of obtaining homogeneous metal parts with high relative density, the influence of post-processing parameters, sintering and reduction temperatures on the final microstructures were studied. Firstly, the sintered metal oxide components enhanced mechanical strength to the part and demonstrate that MVP-VPP printed metal parts can be obtained with good morphology and porosity after thermal

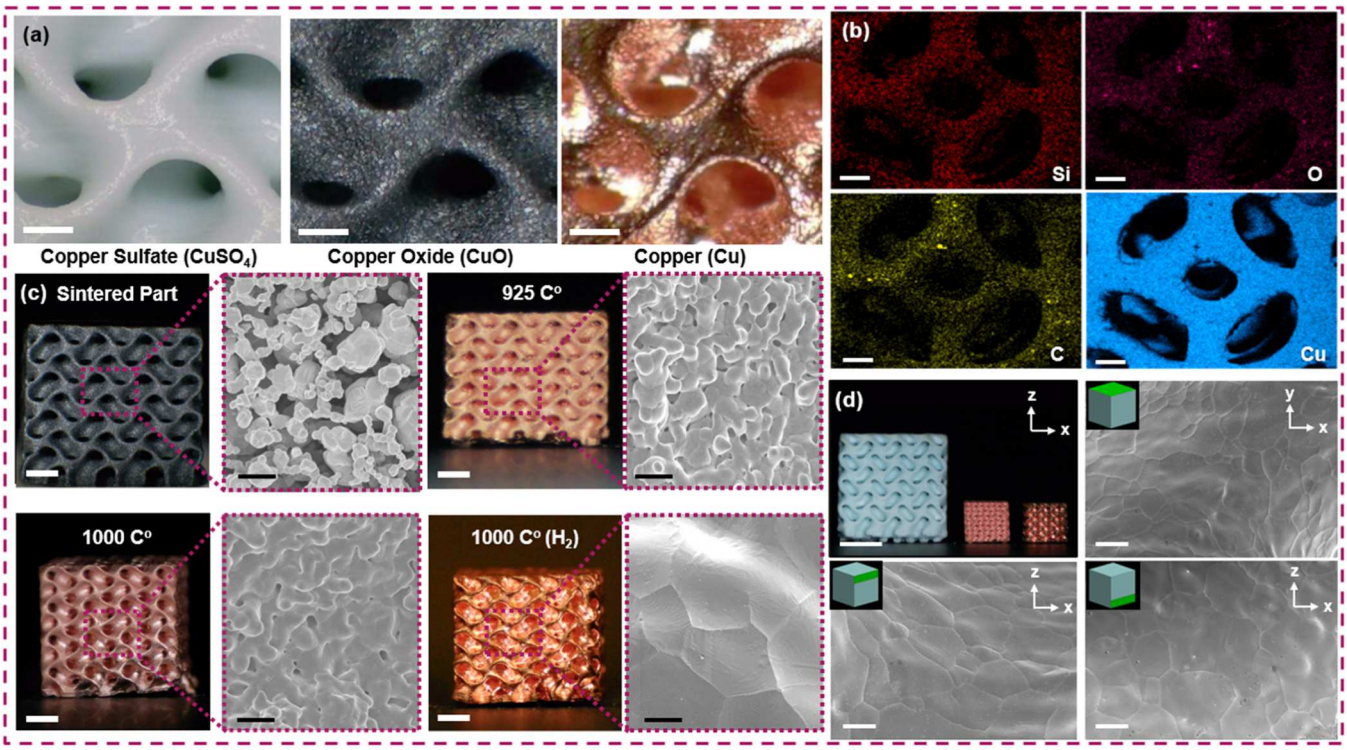

Fig. 4. Thermal post-processing of 3D printed metal precursors (a) showing the thermal decomposition of embedded $CuSO_4$ to CuO followed by thermal reduction to Cu; (b) SEM images of elemental mapping; (c) influence of sintering temperatures on metallic microstructures; (d) isotropic evaluation of front, top, and bottom surfaces after linear shrinkage. Scale bars (a) left to right – 1 mm, 500 μm, and 500 μm; (b) 500 μm; (c) 1 mm (microscope image), 2 μm (SEM image of sintered part), and 10 μm (SEM images of metallic part); (d) 4 mm (microscopic images) and 20 μm (SEM images).

processing, see Fig. 4c. SEM images of the Cu gyroid sintered at 925° C and 1000° C exhibit slightly distinct levels of porosity within the microstructures for the same reducing conditions. The printed Cu gyroid sintered at 1000° C shows that the particles within the microstructures are more tightly packed together since the particles were densified at a higher temperature. Conversely, high relative density microstructures, with the uniform grain size, can be seen in the final Cu gyroid by simply increasing the H_2 reduction temperature to 1000° C. Because both the sintering and reduction temperatures were increased, the final Cu gyroid displayed well defined grain boundaries with no observable porosity, see Figure S4**.** Furthermore, the luster seen in Cu gyroids increases for higher sintering and reduction temperatures since the gyroid at 925° C has a slight orange hue in comparison to the 1000° C gyroid which exhibits a pink hue. Additionally, higher reduction temperatures shift the luster of the Cu gyroid to a dark-orange hue; however, if the part is exposed to high temperatures and flow rate of H_2 for long dwell times, the onset of hydrogen embrittlement will deteriorate the Cu parts. This opens intriguing perspectives since the microstructures of the monolithic metal part can be controlled by modulating the sintering and reduction temperature profiles.

3.3.3. *Evaluation of shape changing and isotropic properties*

At each stage of the thermal decomposition process, MVP-VPP printed part maintains its morphology and surface quality, predefined by the continuous mask video projection during fabrication, by dispersant and polymer removal, metal oxide formation, sintering, and metal oxide reduction (see Figure S3). During metal oxide formation and sintering, the feature size of the gyroid design is reduced while annealing CuO particles and undergoes linearly shrinkage by ~36 % followed by another significant decrease in dimension after metal oxide reduction. After post-processing, the overall linear shrinkage of the printed gyroid lattice is ~59 %, as shown in Fig. 4d. Consequently, precise dimensional control can be achieved, considering the uniform shrinkage during the design and fabrication phase, to obtain geometrically complex metal structures with microscale feature sizes that significantly exceed the printing resolution of the MVP-VPP printer. Furthermore, SEM images of the front and top side of the final gyroid lattice display uniform grain distribution, with high density throughout the microstructures, indicating that metal structures printed via MVP-VPP are monolithic and homogeneous. Additionally, the surface quality is significantly improved, in comparison to layer-based AM approaches, with no observable staircasing effect. Therefore, these results are highly advantageous since it suggests that metal parts fabricated via the MVP-VPP process have isotropic physical properties, which can significantly enhance the performance of 3D printed functional metal devices.

3.4. *Performance evaluation of MVP-VPP metal parts*

3.4.1. *Evaluation of functional metal devices printed via MVP-VPP*

Fundamentally different from traditional layer-based metal 3D printing technologies, the MVP-VPP process has the ability to fabricate sophisticated and unique functional metal devices, within a matter of minutes, with improved physical performance and excellent surface roughness that can be useful for various applications. Metal salt resin with 62 % (w/w) solid loading were utilized to fabricate metal parts for diverse purposes. Fig. 5a shows an intricately designed heat sink fabricated through the MVP-VPP process before and after thermal post-processing. It can be observed that even for cylindrical or columnar structures the overall morphology is maintained, and shrinkage is uniform throughout the entire part. Furthermore, SEM images show that the Cu heat sink has an extremely smooth surface finish, with minimal layer adhesion between adjacent layers, leading to more homogeneous thermal conduction and more efficient heat dissipation. Similarly, a conical horn antenna (Fig. 5b) was designed and fabricated through the MVP-VPP process and exhibits a dense microstructure, with smooth

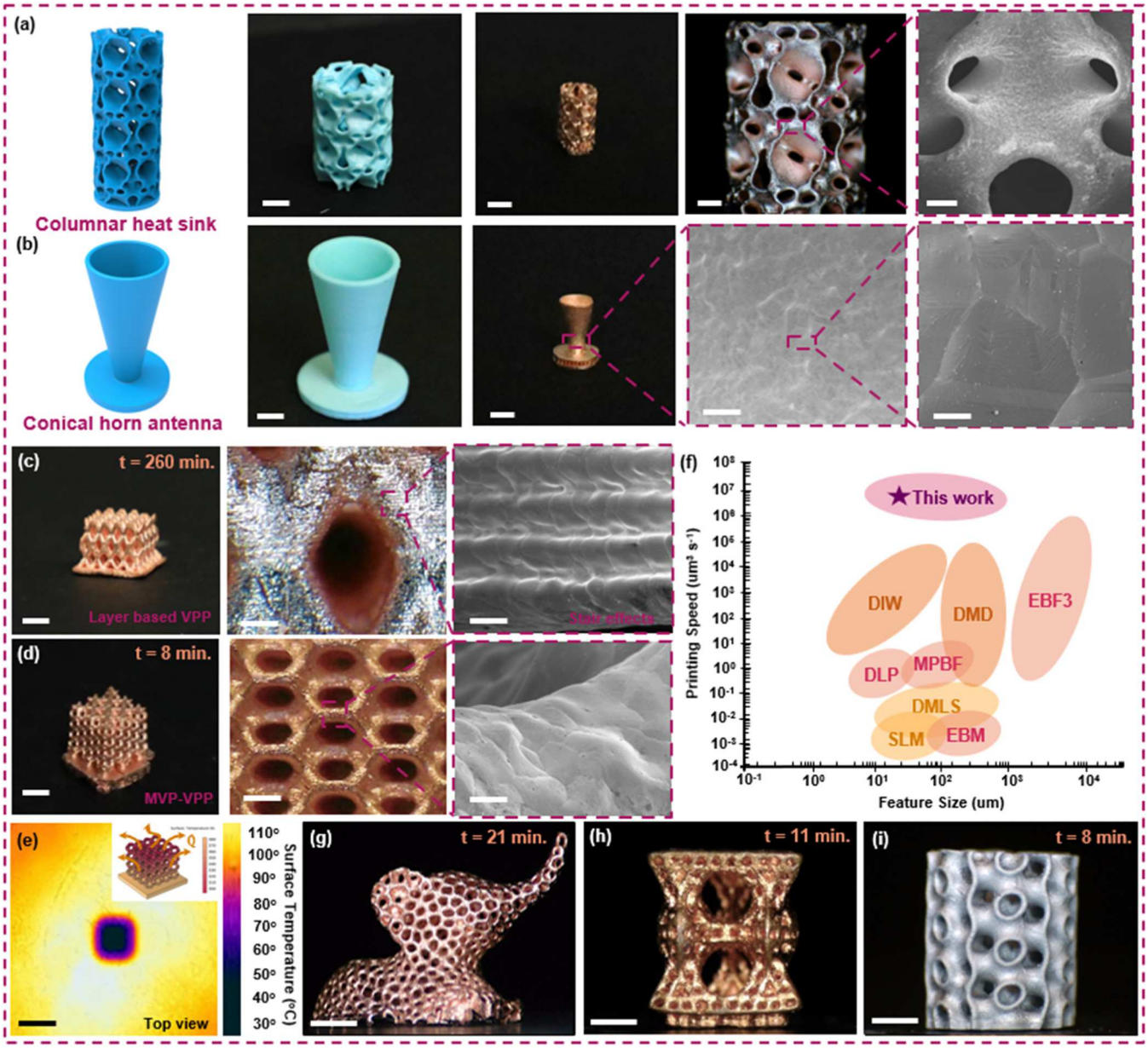

Fig. 5. Performance evaluation of metallic parts printed via MVP-VPP process (a) bioinspired columnar heat sink fabrication overflow from digital model to final parts; (b) conical horn antenna fabrication overflow from digital model to final parts; (c) layer-based VPP and (d) layerless MVP-VPP printed Cu lattice structures; (e) thermal distribution of continuous MVP-VPP printed heat sink with inset of simulation; (f) printing speed comparison with traditional metal AM techniques; (g) Cu elephant (21 minutes); (h) kagome space tower (11 minutes); and (i) Iron columnar gyroid. Scale bars: (a) left to right – 2 mm, 2 mm, 1 mm, 200 μm; (b) left to right – 2 mm, 2 mm, 30 μm, 5 μm; (c) left to right – 1 mm, 500 μm, 20 μm; (d) left to right – 1 mm, 500 μm, 10 μm; (e) 4 mm; (g) 5 mm; (h) 2 mm; (i) 2 mm.

surface roughness, as depicted in SEM images. The high density, uniform distribution of grains, and superior surface roughness are necessary for robust antenna design applications that require strict design tolerances to minimize electrical loss and optimize the transmission signal for a designated frequency range. Moreover, the printing method demonstrates cost-effectiveness and environmental friendliness when compared to traditional metal AM technologies, showcasing an overall cost reduction of approximately 99.3 % (refer to Table S1 in the Supporting Information). Additionally, it enables the recycling of metal objects by dissolving them in acid and drying to recover sulfate crystals. In comparison to traditional metal AM methods, the overall print times and cost are significantly improved, which enables the rapid prototyping and iterative design of functional metal devices with microscale resolution.

3.4.2. *Comparison with layer-based 3D printing and property characterization*

In order to assess the speed and physical performance of metal parts fabricated via the MVP-VPP process, the printing times and microstructures of a layer-based and layerless VPP printed heat sink were compared. As shown in Fig. 5c, a lattice heat sink, with X-type unit cell of dimensions 1 mm×1 mm x 2.5 mm, requires a total printing time of 260 minutes, using layer based VPP with 20-micron slicing thickness, to obtain the metal precursors. Moreover, microscopic images of the surface quality demonstrate that even at thin slicing thickness the layer-effect from curing a single layer is clearly visible which drastically impacts the surface quality of the final metal part. Moreover, SEM images evince that layer-based printing approaches inherently result in dense microstructures, same to our continuous printing approach, however the bonding between individual layers results in anisotropic physical

properties where the metal part is heterogeneous and composed of hundreds of layers. Conversely, a lattice heat sink, with Kelvin unit cell and same z-height as the X-type cell of 12.5 mm, exhibits significantly improved surface roughness when it was printed using our proposed method compared with the layer-based X-type lattice, and the printing speed is substantially reduced to only 8 minutes, which is a 97 % decrease in fabrication time, see Fig. 5d. Thermal management devices printed through this MVP-VPP process therefore are more advantageous since the thermal properties of a particular design can be rapidly fabricated and tested in a short amount of time without the need for expensive manufacturing equipment and material.

Thermal characterization of the MVP-VPP printed Kelvin heat sink was conducted utilizing COMSOL Multiphysics and experimental testing to determine the heat dissipation capabilities of the final printed heat sink. The simulation and experimental boundary condition of T=110 ° C is imposed on the bottom plate of the heat sink and the environmental conditions of the air are 25 ° C (Figure S6). The thermal distribution of the printed heat sink (see Fig. 5e) illustrates that the metal structures is thermal conductive and highly efficient with the lowest recorded temperature being approximately 40 ° C. Moreover, the front view of the IR images further reveals that the heat dissipation at the outer boundary of the printed Kelvin heat sink is broader than the top view with a distinctive layer of hot, warm air surrounding the structure, see Figure S6. This aligns with thermal simulation results of the digital model shown within the inset of Fig. 5e. Consequently, the MVP-VPP technology can be extended to multiple thermal management systems for optimally designed industrial applications with high printing quality and resolution.

3.4.3. *Printing speed comparison with conventional metal 3D printing*

Conventional metal AM technologies employ various methods in order to supply the necessary energy to form the desired 3D metal objects from raw material such as jetting binder material, laser and electron deposition, and material extrusion layer-by-layer. Because the achievable feature size and build time are closely correlated to the energy deposition method, the overall printing speed of current conventional metal AM is compared with the proposed MVP-VPP process. In this work, the continuous metal AM process is capable of achieving printing speeds exceeding 10^7 $\mu m^3 s^{-1}$ for a feature size of 100 μm in contrast to both energy and material deposition methodologies (**Supporting Video 1**). For example, selective laser melting (SLM), direct metal laser sintering (DMLS), electron beam melting (EBM), and metal powder bed fusion (MPBF) can fabricate 3D metal objects with a similar range of minimum feature size (10–1000 μm), however since the energy deposition tool must trace the tool path for an entire layer, the printing speed is dramatically increasing the overall fabrication time, see Fig. 5f [32–34]. The same trend can be seen for material extrusion methods, such as direct ink writing (DIW), direct metal deposition (DMD), and freeform electron beam fabrication (EBF3) [33–35]. The printing speed is significantly improved by the linear printing speed of the printing nozzle, since material is directly deposited onto the build platform, to form an individual layer, but consequently the build time is limited by the predefined tool path. Furthermore, many metals and alloys can potentially be printed using this technique if the metal salts can undergo oxidation and reduction reactions to form the corresponding metals. For example, iron (from iron chloride or sulfate), silver (from silver nitrate), zinc (from zinc sulfate), and nickel (from nickel sulfate or chloride) can be fabricated using the MVP-VPP process. By adjusting the types of inorganic metal salts in the printing resin and optimizing post-processing parameters based on TGA results of the green body samples, pure metals/alloys can be formed. Utilizing the proposed MVP-VPP approach, complex structures such as a Voronoi elephant (Fig. 5g), a Kagome tower (Fig. 5h), and a columnar iron gyroid (Fig. 5i) can be fabricated in just 21 minutes, 11 minutes, and 8 minutes, respectively. In contrast, these structures would take hours to produce using the traditional VPP printing approach.

4. Conclusion

In summary, this work introduced an innovative and cost-effective continuous metal AM technology that excels in producing highly dense and uniformly structured metal objects at significantly improved printing speeds and surface quality compared to conventional metal AM methods. This achievement is made possible by dispersing metal salts into monomer and dispersant photocurable solutions, creating low-viscosity printing inks that exhibit excellent printability. The liquid phase of printing resin with low viscosity and even distribution of metal salt efficiently transports metal salt to the printing area, ensuring complex geometries can be continuously produced. Moreover, the continuous nature of the process, achieved through high-frame-rate video projection from digital models, results in substantially enhanced surface quality, free from the conspicuous staircasing effect seen in layer-based metal AM technologies. The impact of printing speed and resin recoating during the printing has been thoroughly explored, and mathematical models have been developed to predict optimal printing speeds. This metal fabrication approach involves the thermal decomposition of printed metal precursors to form hierarchically porous metal oxide structures, which are then reduced to create dense metal objects. During this transformation, there is a linear shrinkage of approximately 59 % in size. Notably, the proposed process achieves printing speeds that are 5–8 orders of magnitude faster than traditional metal AM methods with same feature printing resolution. Moreover, this printing method demonstrates cost-effectiveness and recyclability in comparison to traditional metal AM technologies, with an overall cost reduction of approximately 99.3 %. This innovation opens up exciting possibilities for the low-cost fabrication of mesoscale and microscale 3D metal objects, characterized by excellent surface roughness and isotropic physical properties, even in highly complex geometries. We believe that this proposed metal AM process will catalyze research efforts aimed at enhancing the speed of metal rapid prototyping technologies, with broad-reaching applications in aerospace, electronics, and the biomedical industries, thereby propelling advancements in these sectors.

CRediT authorship contribution statement

Dylan Joralmon: Writing – original draft, Methodology, Investigation, Formal analysis, Data curation. **Tengteng Tang:** Writing – original draft, Investigation, Data curation. **Sriram Rama Prakash:** Data curation. **Xiangjia Li:** Writing – review & editing, Supervision, Project administration, Funding acquisition, Conceptualization. **Harsh Verma:** Data curation. **Stephanie Kim:** Data curation.

Declaration of Competing Interest

The authors declare the following financial interests/personal relationships which may be considered as potential competing interests: Xiangjia Li reports financial support was provided by National Science Foundation. If there are other authors, they declare that they have no known competing financial interests or personal relationships that could have appeared to influence the work reported in this paper.

Data availability

Data will be made available on request.

Acknowledgements

We gratefully acknowledge the use of facilities within the Center for Solid State Science at Arizona State University, Dr. Kailong Jin's research group for use of their instruments, and Zishuo Zhao and Dr. Linqin Mu's research lab for use of their furnace. The authors acknowledge ASU Startup Funding, ASU NEI-STC-MADE Funding, National Science Foundation (NSF grant no. CMMI-2114119, CMMI-

2338752) and the ASU core research facilities for the use of all instruments.

Supporting Information

Supporting Information is available from the Wiley Online Library or from the author.

Appendix A. Supporting information

Supplementary data associated with this article can be found in the online version at doi:10.1016/j.addma.2024.104314.

References

[1] C. Panwisawas, Y.T. Tang, R.C. Reed, Metal 3D printing as a disruptive technology for superalloys, Nat. Commun. 11 (1) (2020) 2327.
[2] S.C. Joshi, A.A. Sheikh, 3D printing in aerospace and its long-term sustainability, Virtual Phys. Prototyp. 10 (4) (2015) 175–185.
[3] K. Moeinfar, et al., A review on metallurgical aspects of laser additive manufacturing (LAM): Stainless steels, nickel superalloys, and titanium alloys, J. Mater. Res. Technol. 16 (2022) 1029–1068.
[4] C. Guo, et al., Additive manufacturing of Ni-based superalloys: Residual stress, mechanisms of crack formation and strategies for crack inhibition, Nano Mater. Sci. 5 (1) (2023) 53–77.
[5] X. Wang, et al., *3D printing externally reinforced layers for high-speed railway brake discs: Adaptability of SLM processes for manufacturing gradient materials.* Materials Today, Communications 31 (2022) 103778.
[6] B. Blakey-Milner, et al., Metal additive manufacturing in aerospace: A review, Mater. Des. 209 (2021) 110008.
[7] Y. Zhu, et al., 3D printing biomimetic materials and structures for biomedical applications, Bio-Des. Manuf. 4 (2021) 405–428.
[8] S.P. Murray, et al., A defect-resistant Co–Ni superalloy for 3D printing, Nat. Commun. 11 (1) (2020) 4975.
[9] J. Yang, et al., Laser 3D printed bio-inspired impact resistant structure: failure mechanism under compressive loading, Virtual Phys. Prototyp. 15 (1) (2020) 75–86.
[10] Y. Li, et al., A review on functionally graded materials and structures via additive manufacturing: from multi-scale design to versatile functional properties, Adv. Mater. Technol. 5 (6) (2020) 1900981.
[11] L. Yan, Y. Chen, F. Liou, Additive manufacturing of functionally graded metallic materials using laser metal deposition, Addit. Manuf. 31 (2020) 100901.
[12] J. Pragana, et al., *Hybrid metal additive manufacturing: A state–of–the-art review.* Advances in Industrial and Manufacturing Engineering 2 (2021) 100032.
[13] Z.-C. Fang, et al., Review on residual stress in selective laser melting additive manufacturing of alloy parts, Opt. Laser Technol. 129 (2020) 106283.
[14] E. Maleki, et al., Surface post-treatments for metal additive manufacturing: Progress, challenges, and opportunities, Addit. Manuf. 37 (2021) 101619.
[15] Y. Kok, et al., Anisotropy and heterogeneity of microstructure and mechanical properties in metal additive manufacturing: A critical review, Mater. Des. 139 (2018) 565–586.
[16] Y. Zhang, et al., Additive manufacturing and characterization of microstructure evolution of Inconel 718 superalloy produced by vat photopolymerization, Addit. Manuf. 61 (2023) 103367.
[17] X. Zan, et al., Three-dimensional porous tungsten via DLP 3D printing from transparent ink, J. Phys. D: Appl. Phys. 55 (44) (2022) 444004.
[18] C. Li, et al., Stereolithography of 3D Sustainable Metal Electrodes towards High-Performance Nickel Iron Battery, Adv. Funct. Mater. 32 (40) (2022) 2205317.
[19] J.R. Tumbleston, et al., Continuous liquid interface production of 3D objects, Science 347 (6228) (2015) 1349–1352.
[20] X. Li, et al., Mask video projection-based stereolithography with continuous resin flow, J. Manuf. Sci. Eng. 141 (8) (2019) 081007.
[21] G. Lipkowitz, et al., Injection continuous liquid interface production of 3D objects, Sci. Adv. 8 (39) (2022) eabq3917.
[22] A.A. Bhanvadia, et al., High-resolution stereolithography using a static liquid constrained interface, Commun. Mater. 2 (1) (2021) 41.
[23] Y. Li, et al., Incorporating metal precursors towards a library of high-resolution metal parts by stereolithography, Appl. Mater. Today 29 (2022) 101553.
[24] C. Ma, et al., Metal-doped polymer-derived SiOC composites with inorganic metal salt as the metal source by digital light processing 3D printing, Virtual Phys. Prototyp. 15 (3) (2020) 294–306.
[25] M.A. Saccone, et al., Additive manufacturing of micro-architected metals via hydrogel infusion, Nature 612 (7941) (2022) 685–690.
[26] H.X. Nguyen, et al., Development of an innovative, high speed, large-scaled, and affordable metal additive manufacturing process, CIRP Ann. 69 (1) (2020) 177–180.
[27] E.B. Joyee, L. Lu, Y. Pan, Analysis of mechanical behavior of 3D printed heterogeneous particle-polymer composites, Compos. Part B: Eng. 173 (2019) 106840.
[28] T.J. Kolibaba, J.P. Killgore, B.W. Caplins, C.I. Higgins, U. Arp, C.C. Miller, D. L. Poster, Y. Zong, S. Broce, T. Wang, V. Talačka, J. Andersson, A. Davenport, M. A. Panzer, J.R. Tumbleston, J.M. Gonzalez, J. Huffstetler, B.R. Lund, K. Billerbeck, X. Zhao, Results of an interlaboratory study on the working curve in vat photopolymerization, Addit. Manuf. 84 (2024) 104082.
[29] G.K. Batchelor, An Introduction to Fluid Dynamics, Cambridge university press, 1967.
[30] G. Odian, Principles of Polymerization, John Wiley & Sons, 2004.
[31] Jacobs, P.F., *Rapid prototyping & manufacturing: fundamentals of stereolithography*. 1992: Society of Manufacturing Engineers.
[32] L. Hirt, et al., Additive manufacturing of metal structures at the micrometer scale, Adv. Mater. 29 (17) (2017) 1604211.
[33] K. Karunakaran, et al., Rapid manufacturing of metallic objects, Rapid Prototyp. J. 18 (4) (2012) 264–280.
[34] A. Vyatskikh, et al., Additive manufacturing of 3D nano-architected metals, Nat. Commun. 9 (1) (2018) 593.
[35] A.E. Jakus, et al., Metallic architectures from 3D-printed powder-based liquid inks, Adv. Funct. Mater. 25 (45) (2015) 6985–6995.
[36] X. Li, et al., 3D printing temporary crown and bridge by temperature controlled mask image projection stereolithography, Procedia Manuf. 26 (2018) 1023–1033.
[37] Li, X., et al. *Multi-scale additive manufacturing: an investigation on building objects with macro-, micro-and nano-scales features*. in 11th International Conference on Micro Manufacturing, *Irvine, CA*, 2016.